# Mo<sub>6</sub>S<sub>3</sub>Br<sub>6</sub>: An Anisotropic 2D Superatomic Semiconductor

Xinjue Zhong, Kihong Lee, Daniele Meggiolaro, Avalon H. Dismukes, Bonnie Choi, Feifan Wang, Colin Nuckolls, Daniel W. Paley, Patrick Batail, Filippo De Angelis, Xavier Roy,\* and Xiaoyang-Y. Zhu\*

Two-dimensional (2D) van der Waals materials with in-plane anisotropy are of great interest for directional transport of charge and energy, as exemplified by recent studies on black phosphorus and  $\alpha$ -phase molybdenum trioxide ( $\alpha$ -MO<sub>3</sub>). Here, a layered van der Waals semiconductor with in-plane anisotropy built upon the superatomic units of Mo<sub>6</sub>S<sub>3</sub>Br<sub>6</sub> is reported. This material possesses robust 2D characteristics with a direct gap of 1.64 eV, as determined by scanning tunneling spectroscopy and first-principles calculations. Polarization-dependent Raman spectroscopy measurement and density functional theory calculation reveal strong in-plane anisotropy. These results suggest an effective strategy to explore anisotropic 2D electronic and optoelectronic properties from superatomic building blocks with multifunctionality, emergent properties, and hierarchical control.

### 1. Introduction

Two-dimensional (2D) van der Waals materials with in-plane anisotropy are of interest for directional transport of charge and energy. One prominent example is black phosphorus, which has been shown to host highly anisotropic excitons and theoretically predicted to exhibit elliptic and hyperbolic dispersions

X. Zhong, K. Lee, A. H. Dismukes, B. Choi, F. Wang, C. Nuckolls, P. Batail, X. Roy, X.-Y. Zhu Department of Chemistry Columbia University New York, NY 10027, USA E-mail: xr2114@columbia.edu; xyzhu@columbia.edu Dr. D. Meggiolaro, Prof. F. De Angelis Computational Laboratory for Hybrid/Organic Photovoltaics (CLHYO) Via Elce di Sotto 8, I-06123 Perugia, Italy Dr. D. Meggiolaro, Prof. F. De Angelis D3-CompuNet Istituto Italiano di Tecnologia Via Morego 30, 16163 Genova, Italy Dr. D. W. Paley Columbia Nano Initiative Columbia University New York, NY 10027, USA Prof. P. Batail Laboratoire MOLTECH CNRS UMR 6200 Université d'Angers 49045 Angers, France

The ORCID identification number(s) for the author(s) of this article

can be found under https://doi.org/10.1002/adfm.201902951.

DOI: 10.1002/adfm.201902951

for plasmon polaritons. [1–3] Likewise, inplane anisotropy in  $\alpha$ -phase molybdenum trioxide ( $\alpha$ -MoO<sub>3</sub>) has been demonstrated to yield ultra-low-loss phonon polaritons. [4] Besides, in rhenium dichalcogenides, [5] the in-plane anisotropy [6] can be used to fabricate unique photodetectors and filed-effect transistors. [7] When compared to traditional 2D atomic solids, however, the structural diversity combined with in-plane anisotropy is limited, which has restricted their use.

Beyond atomic solids, there is a growing interest in designing 2D materials from complex, hierarchical, and tunable building blocks, [8] as exemplified by colloidal nanoparticle 2D superlat-

tices. [9–11] The use of zero-dimensional building blocks formed by atomic clusters, known as superatoms, is particularly attractive and advantageous due to their atomic precision, as well as the tunability of intercluster coupling. [12–14] Their assembly into strongly coupled hierarchical lattices has been shown to produce unique emergent material properties. For instance, three-dimensional (3D) cluster-assembled solids such as Chevrel phases [15] and endohedral gallide cluster phases [16] are well-known for their superconducting behaviors. In view of this, 2D structures with in-plane anisotropy promise unique physical properties and functions. However, there are very few examples of layered cluster-based structures [17–19] that can be exfoliated, and the existing ones typically have isotropic in-plane structures (e.g., Re $_6$ Se $_8$ Cl $_2$ ). [20–22]

Here, we investigate Mo<sub>6</sub>S<sub>3</sub>Br<sub>6</sub>, a superatomic van der Waals material with strong in-plane anisotropy derived from the Chevrel phase in which [Mo<sub>6</sub>] octahedral cluster subunits are covalently linked into layers.<sup>[19,23]</sup> Each [Mo<sub>6</sub>] octahedron is tilted, enclosed in a cube of sulfur (S) and bromine (Br), and connected to two neighboring clusters along the c-axis via a shared S atom located at the apical positions as well as via an additional two bridging Br atoms (Figure 1a). The resulting corner-sharing one-dimensional (1D) chains of clusters are linked into layers in the bc-plane by means of two interchain Mo-S linkages along the b-axis. The clusters form in such a way that the S atoms are inside the layers and the Br atoms are at the surface, establishing the van der Waals planes. The weak van der Waals contacts between the layers along the a-axis and strong in-plane bonding give this material a robust 2D character with stronger coupling along the *c*-axis.

Mo<sub>6</sub>S<sub>3</sub>Br<sub>6</sub> was discovered in 1983 by Perrin et al.,<sup>[23]</sup> but its bulk physical properties are essentially unknown, and it has

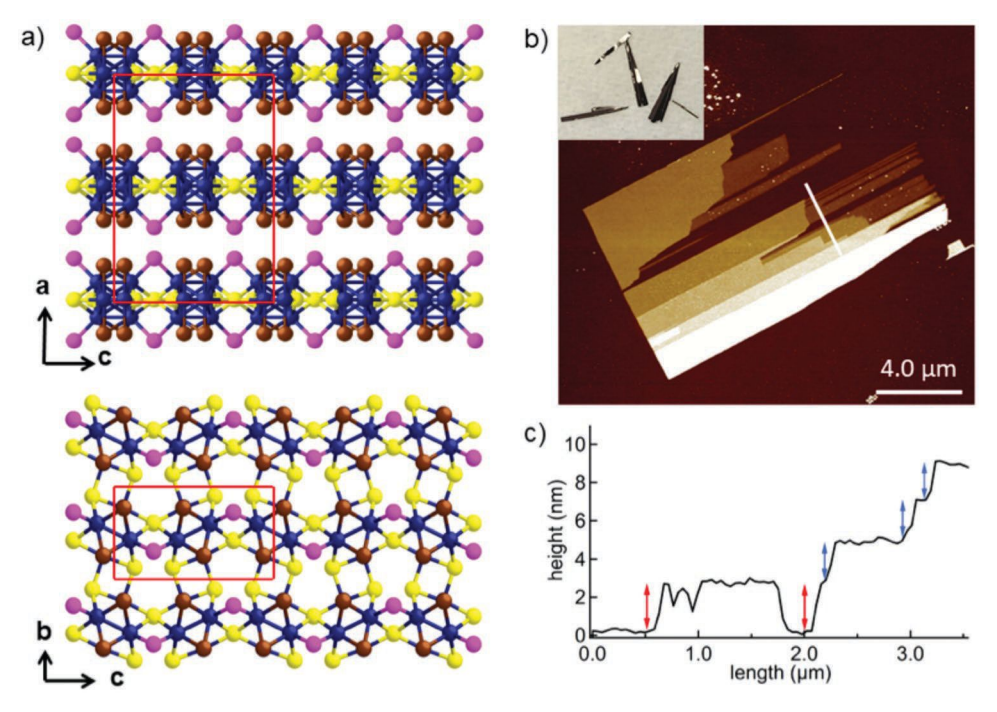


Figure 1. a) Crystal structure of Mo<sub>6</sub>S<sub>3</sub>Br<sub>6</sub>. Side view (top) of the *ac*-plane and top view (bottom) of the *bc*-plane. Unit cells are marked by the red boxes. One directional chain is along *c*-axis. Color code: Mo, blue; S, yellow; Br, brown (innercluster) and pink (intercluster bridging). b) AFM image on an exfoliated Mo<sub>6</sub>S<sub>3</sub>Br<sub>6</sub> flake on a SiO<sub>2</sub>/Si substrate. Top inset: optical image ( $\approx$ 3 mm  $\times$  2 mm) of the macroscopic Mo<sub>6</sub>S<sub>3</sub>Br<sub>6</sub> crystals. c) The height profile along the white line in (b). The thickness of the first layer and the sequential layers is marked by red and blue arrows, respectively.

never been investigated as a mono- or few-layer material. One obstacle to such studies is that Mo<sub>6</sub>S<sub>2</sub>Br<sub>6</sub> is typically obtained as small crystals (tens of micrometers), precluding mechanical exfoliation. In this work, we report a new synthetic approach to grow millimeter-size single crystals of Mo<sub>6</sub>S<sub>3</sub>Br<sub>6</sub> that can be mechanically exfoliated. We focus on freshly cleaved surfaces of bulk crystals in all experiments based on scanning tunneling microscopy/spectroscopy (STM/STS) and polarization dependent Raman spectroscopy combined with first-principles calculations. We demonstrate the strong in-plane anisotropic electronic structure. Density functional theory (DFT) calculations support the pseudo-1D electronic structure of this material and reveal a direct bandgap with the valence band maximum (VBM) and the conduction band minimum (CBM) located at the Y (0, 0.5, 0) point in momentum space. The electronic bandgap determined by STS is 1.64 eV, with the Fermi level ( $E_{\rm F}$ ) located 0.21 eV above the VBM, indicating p-type doping.

### 2. Results and Discussions

We synthesized microcrystalline  $Mo_6S_3Br_6$  by heating a stoichiometric mixture of  $Mo_6Br_{12}$ , Mo, and S to 1175 °C in a fused silica tube sealed under vacuum. Remarkably, millimeter-size crystals (shown in the inset of Figure 1b) are obtained when a mixture of Mo and Mo (in a molar ratio of 92.5:7.5) is used instead of the pure Mo metal. In addition to microcrystalline  $Mo_6S_3Br_6$  powder and macroscopic crystals, the tube contains a few crystals of  $NbBr_5$ , which form in situ and presumably acts as a chemical vapor transport agent that allow large  $Mo_6S_3Br_6$  crystals to grow. The flattened needle morphology

of these crystals indicates different growth rates along the b- and c-axes, consistent with the anisotropic in-plane structure (inset of Figure 1b). The structure of the  $Mo_6S_3Br_6$  crystals was determined by single-crystal X-ray diffraction (SC-XRD). In agreement with previous reports, the structure is orthorhombic (space group: Cmcm), with lattice parameters a=17.27 Å, b=6.58 Å, c=11.90 Å at 297 K and c-axis corresponds to the elongated direction of the crystal (Figure S1, Supporting Information). Variable temperature SC-XRD measurements between 100 and 297 K show monotonic increase of the lattice due to thermal expansion, with no structural phase transitions (Figure S2, Supporting Information). The composition of  $Mo_6S_3Br_6$  crystals was confirmed by energy dispersive X-ray spectroscopy (Table S2, Supporting Information) and X-ray photoelectron spectroscopy (Figure S3, Supporting Information).

To demonstrate the feasibility of Mo<sub>6</sub>S<sub>3</sub>Br<sub>6</sub> as a practical 2D material, we first mechanically exfoliated macroscopic crystals using the Scotch tap method<sup>[24]</sup> and determined the thicknesses of the resulting rectangular flakes by atomic force microscopy (AFM) under ambient conditions. The thinnest flakes obtained using this approach are bilayers (Figure 1b) with thickness of ≈2.5 nm (marked by red arrows in Figure 1c) and sequential steps along the line profile are 2.1 nm on average (marked by blue arrows in Figure 1c), close to the height of two monolayers based on the SC-XRD data (≈1.8 nm). The apparent difference between the height measured by AFM and the SC-XRD data is mainly due to the AFM tip-surface interactions, [22,25,26] which overestimate the step height. Based on these exfoliation results, we explore the in-plane structural and electronic anisotropy of the material by conducting all measurements on freshly cleaved surfaces of bulk Mo<sub>6</sub>S<sub>3</sub>Br<sub>6</sub>. We emphasize that the AFM

www.advancedsciencenews.com www.afm-journal.de



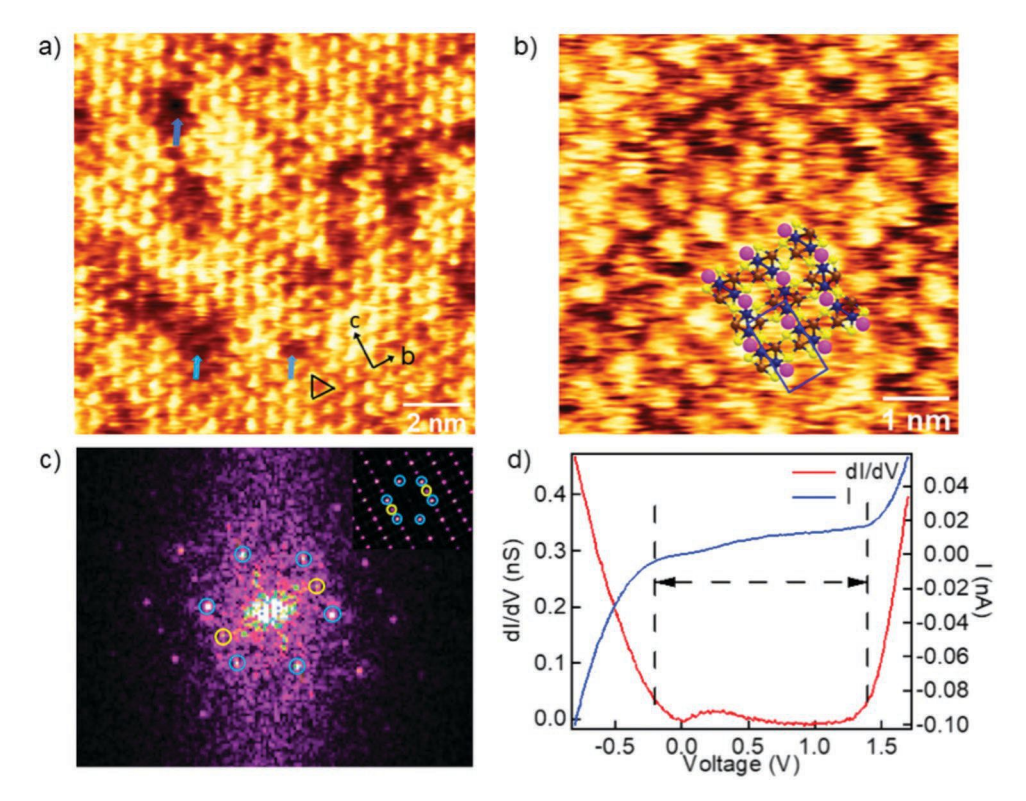


Figure 2. a) High-resolution STM image of  $Mo_6S_3Br_6$  at 298 K (12 × 12 nm, U = 1.6 V, I = 60 pA). c- and b-axes are marked by the black arrows. Several types of defects are identified by the blue arrows. b) Zoom in STM image with overlaid atomic structures. The unit cell is marked by the rectangular box. c) Fast Fourier transform (FFT) of (a). Inset is the simulated FFT of the top layer of Br atoms. d) STS spectrum with I-V curve in blue and the dI/dV-V curve in red. The VBM and CBM are marked by the black dashed lines, giving a bandgap of 1.64  $\pm$  0.05 eV.

measurement serves to confirm the layered nature of the van der Waals crystal. Here, we focus on freshly cleaved surface of bulk  $Mo_6S_3Br_6$  single crystals, not monolayers.

We carried out real-space imaging of the (100) surface structure of Mo<sub>6</sub>S<sub>3</sub>Br<sub>6</sub> using STM. The high-resolution STM image in Figure 2a features the bright spots arranged in a triangular pattern with periodicity of 6.5, 6.6, and 7.0 Å. These bright spots correspond to the positions of the intercluster bridging Br atoms, which are protruding from the plane of the layer (represented as pink spheres in Figure 1a,b). The Br atoms located at the vertex of the [Mo<sub>6</sub>S<sub>4</sub>Br<sub>4</sub>] clusters are topographically lower than the bridging Br atoms, and thus are not clearly resolved in the STM (represented as brown spheres in Figures 1a and 2b). A first Fourier transform (FFT) of the image (Figure 2c) identifies the pseudo sixfold symmetry of the bridging Br atoms. Two more points (identified as yellow circles in Figure 2c) indicates a periodicity of 5.9 Å along one direction, in excellent agreement with the c lattice parameter determined from SC-XRD  $(c/2 \approx 5.97 \text{ Å})$ . By comparing the simulated FFT calculated from the bridging Br atom lattice (inset in Figure 2c) with the experimental data, we determine the b [010] and c [001] directions (represented as black arrows in Figure 2a and as a box in Figure 2b). In addition to the crystal surface structure, we identify several types of defects in Figure 2a, including missing Br atoms or incomplete clusters. More details are included in Figure S4 of the Supporting Information.

We determine the single-particle electronic structure by current–voltage (I–V) measurement in STS. Figure 2d displays I–V

(blue) and dI/dV-V (red) curves. Each I-V or dI/dV-V curve is an average of over 80 curves under the same tunneling conditions at multiple positions on the surface. The VBM is located at  $-0.20 \pm 0.03$  V and the CBM at 1.44  $\pm 0.03$  eV. These give the electronic bandgap  $E_G = E_{CBM} - E_{VBM} = 1.64 \pm 0.05$  eV; this value comes from the average measurements in multiple areas on three samples. The positions of the band edges relative to  $E_{\rm F}$  indicates p-doping. A weak and broad mid-gap feature near  $E_{\rm F}$  is attributed to surface defects. Despite the direct bandgap characteristic (see below), we found that photoluminescence emission from the bandgap transition in the current sample is negligibly, likely due to the defect mediated nonradiative recombination. Further experiments are necessary to improve the quality of the crystals. The high density of midgap states also prohibited reliable measurement on intrinsic transport properties.

To support our experimental observations, we performed DFT calculations of the electronic band structure of  $Mo_6S_3Br_6$  using the Perdew–Burke–Ernzherof (PBE) functional<sup>[27]</sup> and refined the calculation with the Heyd–Scuseria–Ernzerhof (HSE06) functional.<sup>[28]</sup> **Figure 3**a displays the PBE bulk electronic band structure (black curves) and HSE06 refinements (blue dots) at selected high-symmetry points in the Brillouin zone. A direct bandgap of 0.90 eV is derived from PBE functional, which typically underestimates bandgaps. The HSE06 band structure, which generally overestimates bandgaps, indicates a direct bandgap of 1.69 eV, slightly above the value determined by STS. Both VBM and CBM locate at Y (0, 0.5, 0) point

www.advancedsciencenews.com www.afm-journal.de

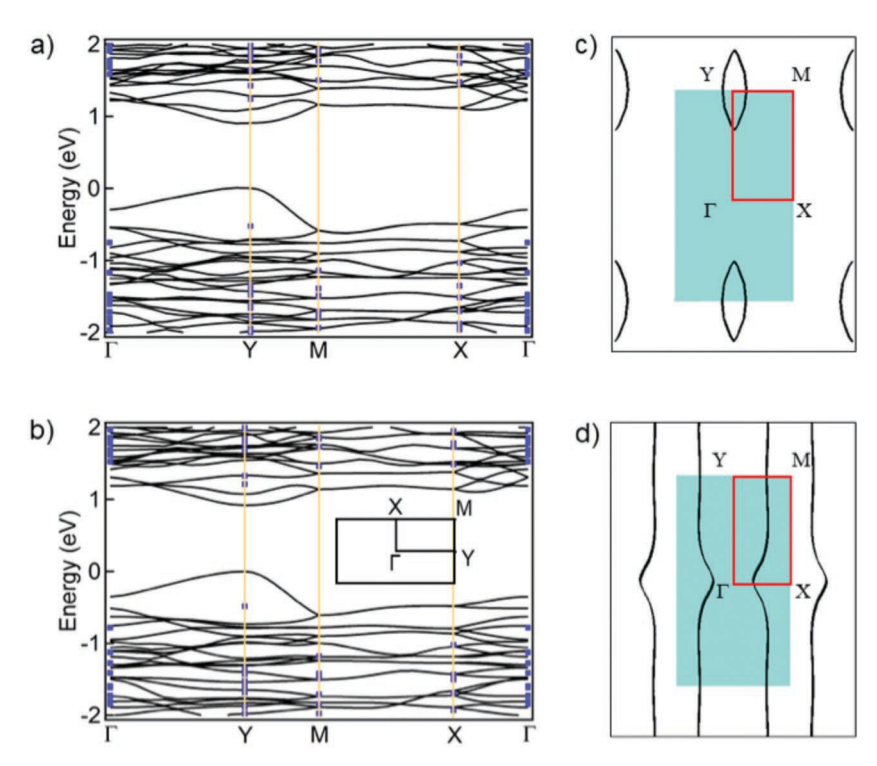


**Figure 3.** a,b) Calculated DFT band structure by using PBE functional (solid black line) and HSE06 functional (blue dots). Inset is the 2D Brillouin zone projected on (100) plane. a) The 3D bulk and b) the 2D monolayer. c) Fermi surface of an intrinsic 2D monolayer. d) Fermi surface of p-doped 2D monolayer with doping level of 0.5 holes per cluster.

in momentum space. To understand the properties of  $Mo_6S_3Br_6$  in the 2D limit, we performed similar calculations on the 2D monolayer, as shown Figure 3b. The electronic band structure of monolayer  $Mo_6S_3Br_6$  is nearly identical to that of the bulk, indicating weak interlayer electronic interactions. The direct bandgaps calculated from PBE and HSE06 functional have the same values at Y (0, 0.5, 0) point as those of the bulk.

Strong anisotropy appears in the band structure along the principal direction  $\Gamma-Y$  (0, 0.5, 0) compared to Y–M (0.5, 0.5, 0). The electronic structure produces two free electron-like bands with starkly different effective masses for electrons and holes, respectively. Similar band structures have been observed in other anisotropic 2D materials, e.g., black phosphorus.  $^{[1,29]}$  The strong in-plane anisotropy is also reflected in the Fermi surface of 2D Mo<sub>6</sub>S<sub>3</sub>Br<sub>6</sub>, both in the intrinsic and doped states. Figure 3c displays the Fermi surface for an intrinsic 2D monolayer. By increasing the doping level to 0.5 hole per cluster, the band along the  $\Gamma-Y$  direction generates pseudo-1D electronic chains (Figure 3d), revealing highly anisotropic electronic properties.

The anisotropic properties of Mo<sub>6</sub>S<sub>3</sub>Br<sub>6</sub> are confirmed experimentally in polarization dependent Raman spectroscopy.<sup>[6,30–34]</sup> **Figure 4**a shows Raman spectra for parallel polarization (PP, top) and cross polarization (CP, bottom) configurations. Spectra were taken in a backscattering geometry, where the incident and scattered light are both perpendicular to the sample. The polarization angle is defined as the angle between the incident polarization and the crystal *c*-axis. Each Raman active mode has either two- or four-fold symmetry governed

by the crystal symmetry. Since Mo<sub>6</sub>S<sub>3</sub>Br<sub>6</sub> has an orthorhombic structure with space group Cmcm, there are 45 Raman active modes  $(13A_g + 11 B_g + 9 B_{2g} + 12 B_{3g})$ , [35] among which 25 modes  $(13A_g + 12 B_{3g})$ are detectable in the backscattering geometry. Raman selection rules dictate that the A<sub>o</sub> mode has twofold symmetry for PP and fourfold symmetry for CP, while B<sub>3g</sub> mode has fourfold symmetry in either PP or CP configurations (details in the Supporting Information). Figure 4b presents parallel-polarized Raman spectra at 0°, 30°, 60°, 90°:15 of the 25 Raman modes are resolved and assigned to  $A_{\rm g}$  or  $B_{3\rm g}$  mode based on DFT calculations (Table S3, Supporting Information). The nonresonant Raman spectrum obtained from DFT calculations is shown in Figure S5 of the Supporting Information as a reference.

To highlight the variations of each peak as a function of angle, Figure 4c,d shows polar plots of two  $A_g$  modes (181.3 and 421.1 cm<sup>-1</sup>) in PP configuration. The Raman intensity of the 181.3 cm<sup>-1</sup>  $A_g$  mode along the *c*-axis is higher than that along the *b*-axis, while the intensity along the *b*-axis shows a secondary maximum instead of a minimum, indicating a complex Raman tensor, as seen in other 2D materials. [36–38]

We performed quantitative analysis of the phonon anisotropy by extracting Raman tensors for  $A_g$  and  $B_{3g}$  modes from the polarization dependent Raman spectra in parallel and cross polarized configurations. The Raman intensity can be expressed as  $I \propto |\epsilon_i R \epsilon_s|^2$ , where  $e_i$  and  $e_s$  are the incident and scattered light vectors and R is the Raman tensor for a specific phonon mode. For incident light perpendicular to the sample (i.e., parallel to the a-axis), the incident light vector  $e_i = (0, \sin\theta, \cos\theta)$  and the scattered light vector  $e_s = (0, \sin\theta, \cos\theta)$  for PP configuration and  $e_s = (0, -\cos\theta, \sin\theta)$  for CP configuration. The Raman tensors of  $A_g$  and  $B_{3g}$  are given by

$$\overrightarrow{R_{A_g}} = \begin{bmatrix} a & 0 & 0 \\ 0 & b & 0 \\ 0 & 0 & c \end{bmatrix}, \quad \overrightarrow{R_{B_{3g}}} = \begin{bmatrix} 0 & 0 & 0 \\ 0 & 0 & f \\ 0 & f & 0 \end{bmatrix}$$

where a, b, c, and f are complex Raman tensor elements. The imaginary parts in the Raman tensor elements can be attributed to photon absorption<sup>[32,33,36,41]</sup> with excitation photon energy above the bandgap and birefringence effects<sup>[42]</sup> along b- and c-axes of the crystals. We obtain the tensor elements of each mode by fitting both parallel and cross polarized Raman spectra simultaneously (details in the Supporting Information). The fits, included in the polar plots in Figure 4c,d as blue solid lines, demonstrate an excellent agreement between experiment and theory. More polar plots of Raman active modes are presented in Figure S6 of the Supporting Information.

The strong in-plane anisotropy of  $Mo_6S_3Br_6$  is also reflected in the separation of the  $A_g$  modes in the PP configuration (Figure 4a): the maximum peak intensity of each  $A_g$  mode

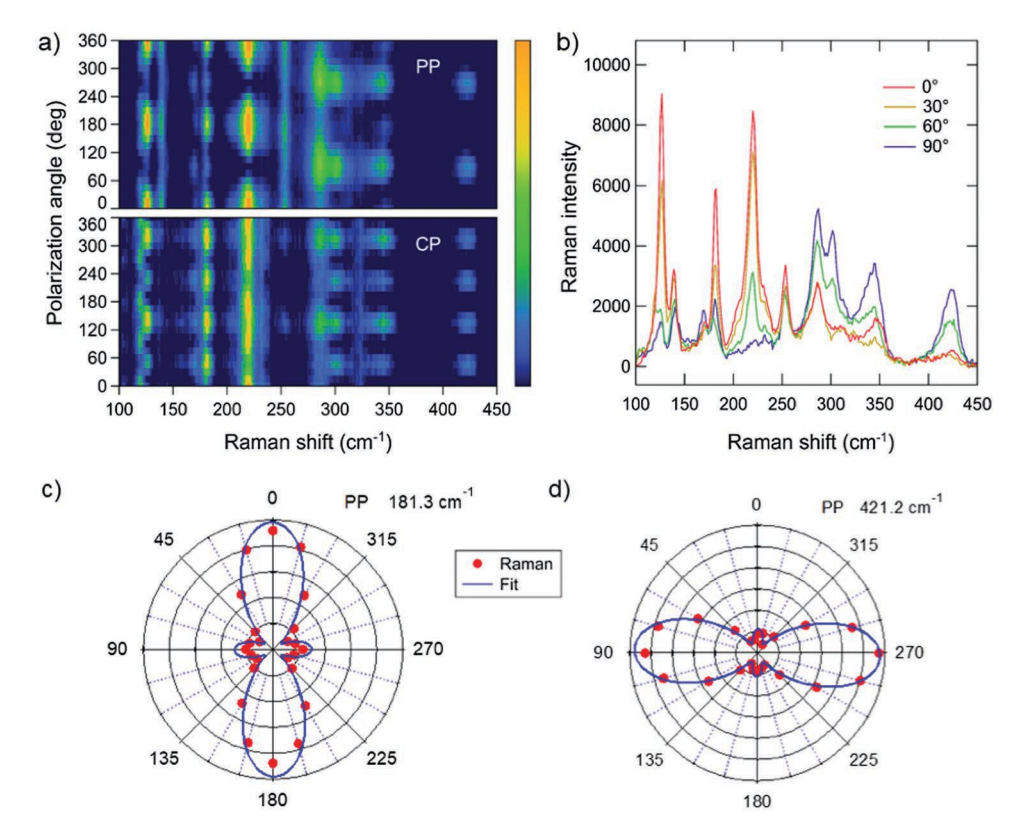


Figure 4. a) Image plots of polarization dependent Raman for parallel polarization (PP) (top) and cross polarization (CP) (bottom).  $0^{\circ}$  angle denotes the c-axis of the crystal. b) Representative parallel-polarized Raman spectra at  $0^{\circ}$ ,  $30^{\circ}$ ,  $60^{\circ}$ , and  $90^{\circ}$ . c) Polar plot of parallel polarized Raman intensity of  $A_g$  mode at 181.3 cm<sup>-1</sup>, showing preferential scattering along the c-axis. d) Polar plot of parallel polarized Raman intensity of  $A_g$  mode at 421.2 cm<sup>-1</sup>, showing strong response along the b-axis.

<270 cm $^{-1}$  is at 0° or 180° while that >270 cm $^{-1}$  is at 90° or 270° (Table S4, Supporting Information). This anisotropy is evident when we compare the polar plots of Ag modes 181.3 and 421.2 cm<sup>-1</sup> shown in Figure 4c,d. This could be understood by taking nuclear motions of each mode into account. Raman active phonons below 270 cm<sup>-1</sup> involves twisting modes of Mo<sub>6</sub> cluster units. Since in those modes two adjacent Mo6 units on the c-axis rotate in opposite directions, the phonons modulate Mo-S bonds of shared  $\mu_6$ -S bridge. This results in strong perturbation of electronically coupled 1D chains of corner-sharing clusters, agreeing with the discussions mentioned above. Phonons above 270 cm<sup>-1</sup> consist of stretching modes of Mo-S bonds. Such vibrations exhibit the strongest effect along the baxis of the crystal, where [Mo<sub>6</sub>] cluster subunits are connected by two Mo—S linkages. The additional sulfur atom on the *b*-axis allows stretching mode phonons to heavily modulate polarizability in that direction, explaining preferential Raman response in b-direction for high-frequency  $A_g$  modes. While there exists Mo-S stretching A<sub>g</sub> mode in c-direction, its Raman crosssection is significantly smaller and not experimentally resolved.

## 3. Conclusion

We have demonstrated that the layered van der Waals cluster solid  $Mo_6S_3Br_6$  is a novel 2D semiconductor with strong inplane anisotropy. This anisotropy is anticipated to produce directional transport of charge and energy, such as carriers, excitons, and polaritons. Moreover, in contrast to most conventional 2D atomic solids, the presence of labile Br atoms at the surface of each 2D  $Mo_6S_3Br_6$  layer may allow the tuning of anisotropic properties by functionalizing their surface via halogen substitution. The unique hierarchical structure of  $Mo_6S_3Br_6$  opens the door to new and exciting optoelectronic devices that combine multifunctionality with in-plane anisotropy.

#### 4. Experimental Section

Synthetic Details:  $Mo_6S_3Br_6$  was prepared in the following procedure, modified from Perrin et al.<sup>[23]</sup> A stoichiometric mixture of  $Mo_6Br_{12}^{[43]}$  (200 mg, 0.13 mmol), S (25 mg, 0.78 mmol), Mo (70 mg, 0.73 mmol), and Nb (6 mg, 0.06 mmol) was ground with a mortar and pestle in an inert atmosphere, pressed into a pellet and sealed in a quartz tube under vacuum. The tube was then heated to 1175 °C in a box furnace with a ramp rate of 1 °C min<sup>-1</sup>, held for 72 h at the reaction temperature, and finally cooled to room temperature at a ramp of 0.5 °C min<sup>-1</sup>. Millimeter-size crystals of  $Mo_6S_3Br_6$  are deposited in the cooler region of the tube.

SC-XRD: Data were collected on an Agilent SuperNova instrument using an MiTeGen Micromount and an Oxford-Diffraction Cryojet system to cool the sample to 100 K. Data collection was performed using CrysAlis Pro while solution and subsequent refinement was done using ShelXT<sup>[44]</sup> and ShelXL,<sup>[45]</sup> respectively. Olex2<sup>[46]</sup> was used to view and prepare CIF files. Table S1 of the Supporting Information includes details of collection parameters and data refinement.



www.advancedsciencenews.com

www.afm-journal.de

ADVANCED FUNCTIONAL MATERIALS

STM/STS: Experiments were carried out on the freshly cleaved  $Mo_6S_3Br_6$  crystal on the Omicron scanning tunneling microscope at room temperature (292 K) in ultrahigh vacuum (base pressure  $<\!4.0\times10^{-10}$  Torr). Images were obtained in the constant-current mode with an electrochemically etched tungsten tip. To avoid tip artifacts, the STM tip was calibrated on a clean Au (111) surface before all measurements. The differential conductance (dI/dV-V) spectra were performed with a lock-in amplifier at an AC modulation of 10 mV and at a frequency of 861.1 Hz. The corresponding current change was acquired by keeping the tip fixed above the surface with the feedback loop off. dI/dV-V spectra are consistent at various spots on the surface with different tips at the same tunneling conditions.

Polarization Dependent Raman: Polarization dependent Raman spectroscopy was performed with a Renishaw microscopic Raman spectrometer. Spectra were taken in a backscattering geometry, where the incident and scattered light are both perpendicular to the sample. A 1 mW 633 nm He-Ne laser was focused on the  $Mo_6S_3Br_6$  surface with ≈1  $\mu$ m spot size. A linear polarizing filter was used in the laser path before the sample for polarization purity, and an additional polarizer was placed between sample and detector to reject cross-polarized light at parallel polarizing configuration. After the polarizing filter within the incident path, a removable half waveplate was placed at a 45° angle between the fast axis and laser polarization, so that the parallel and cross polarizing configurations could be switched with ease. The sample was manually rotated by 15° for each measurement.

Computational Details: DFT calculations were performed on the 3D-bulk and 2D phases of Mo<sub>6</sub>S<sub>3</sub>Br<sub>6</sub>. The Bravais lattice of the bulk system is orthorhombic with room temperature cell parameter a=17.250 Å, b=6.600 Å, c=11.929 Å,  $\alpha=\beta=\gamma=90^{\circ}$  and has 4 formula units (space group 63–Cmcm). Both geometry relaxations and electronic structure calculations were carried out in the primitive cell of Mo<sub>6</sub>S<sub>3</sub>Br<sub>6</sub> (a=b=9.235 Å, c=11.929 Å,  $\alpha=\beta=90^{\circ}$ ,  $\gamma=41.87^{\circ}$ , 2 formula units). The 2D sheet of Mo<sub>6</sub>S<sub>3</sub>Br<sub>6</sub> was modeled in the supercell approach starting from the primitive cell and by introducing 10 Å of vacuum between in-plane layers.

All calculations were carried out in periodic boundary conditions by using plane waves basis set and pseudopotentials. Converged grid of k-points in the Brillouin zone was adopted throughout calculations. Equilibrium structures was found by using Ultrasoft pseudopotentials and the PBE exchange correlation functional<sup>[27]</sup> by relaxing ions positions until a threshold on forces of 0.001 Ry a.u.<sup>-1</sup> was reached. A cutoff on the plane waves of 40 Ry (320 Ry on the charge density) was used. The electronic structure of 3D and 2D systems was further refined by performing single point calculations by using the hybrid HSE06 functional<sup>[28]</sup> at the PBE relaxed geometries. Hybrid calculations were carried out by using Norm-conserving pseudopotentials with a cutoff on the wavefunction of 70 Ry (140 Ry on the Fock grid). All calculations were performed by using the Quantum-Espresso package.<sup>[47]</sup>

#### **Supporting Information**

Supporting Information is available from the Wiley Online Library or from the author.

## Acknowledgements

X.Z. and K.L. contributed equally to this work. Crystal synthesis was supported by the NSF CAREER Award DMR-1751949 to X.R. Sample preparation, characterization, and scanning tunneling spectroscopy/microscopy experiments were supported by the NSF MRSEC program through the Center for Precision Assembly of Superstratic and Superatomic Solids (DMR-1420634). The Raman spectroscopy experiments were supported by the US Air Force Office of Scientific Research (AFOSR) (Grant No. FA9550-18-1-0020). A.H.D. was supported by the NSF Graduate Research Fellowship Program (GRFP)

DGE 16–44869. Single crystal X-ray diffraction, energy dispersive X-ray spectroscopy, and X-ray photoelectron spectroscopy were performed at the Shared Materials Characterization Laboratory at Columbia University. Use of the SMCL was made possible by funding from Columbia University.

#### **Conflict of Interest**

The authors declare no conflict of interest.

#### **Keywords**

2D van der Waals solid, anisotropic phonons, 2D semiconductor

Received: April 11, 2019 Revised: May 8, 2019 Published online: June 11, 2019

- [1] F. Xia, H. Wang, Y. Jia, Nat. Commun. 2014, 5, 4458.
- [2] X. Wang, A. Jones, K. Seyler, V. Tran, Y. Jia, Nat. Nanotechnol. 2015, 10, 517.
- [3] T. Low, R. Roldán, H. Wang, F. Xia, P. Avouris, L. M. Moreno, F. Guinea, Phys. Rev. Lett. 2014, 113, 106802.
- [4] W. Ma, P. Alonso-González, S. Li, A. Y. Nikitin, J. Yuan, J. Martín-Sánchez, J. Taboada-Gutiérrez, I. Amenabar, P. Li, S. Vélez, C. Tollan, Z. Dai, Y. Zhang, S. Sriram, K. Kalantar-Zadeh, S.-T. Lee, R. Hillenbrand, Q. Bao, *Nature* 2018, 562, 557.
- [5] J. C. Wildervanck, F. Jellinek, J. Less-Common Met. 1971, 24, 73.
- [6] D. Wolverson, S. Crampin, A. S. Kazemi, A. Ilie, S. J. Bending, ACS Nano 2014, 8, 11154.
- [7] M. Hafeez, L. Gan, A. S. Bhatti, T. Zhai, Mater. Chem. Front. 2017, 1, 1917.
- [8] D. Jariwala, T. J. Marks, M. C. Hersam, Nat. Mater. 2017, 16, 170.
- [9] R. P. Andres, J. D. Bielefeld, J. I. Henderson, D. B. Janes, V. R. Kolagunta, C. P. Kubiak, W. J. Mahoney, R. G. Osifchin, *Science* 1996, 273, 1690.
- [10] G. Medeiros-Ribeiro, D. A. A. Ohlberg, R. S. Williams, J. R. Heath, Phys. Rev. B 1999, 59, 1633.
- [11] M. P. Boneschanscher, W. H. Evers, J. J. Geuchies, T. Altantzis, B. Goris, F. T. Rabouw, S. A. P. Van Rossum, H. S. J. van der Zant, L. D. A. Siebbeles, G. Van Tendeloo, *Science* 2014, 344, 1377.
- [12] S. A. Claridge, A. W. Castleman, S. N. Khanna, C. B. Murray, A. Sen, P. S. Weiss, ACS Nano 2009, 3, 244.
- [13] E. G. Tulsky, J. R. Long, Chem. Mater. 2001, 13, 1149.
- [14] X. Roy, C.-H. Lee, A. C. Crowther, C. L. Schenck, T. Besara, R. A. Lalancette, T. Siegrist, P. W. Stephens, L. E. Brus, P. Kim, M. L. Steigerwald, C. Nuckolls, *Science* 2013, 341, 157.
- [15] O. Peña, Phys. C 2015, 514, 95.
- [16] W. Xie, H. Luo, B. F. Phelan, T. Klimczuk, F. A. Cevallos, R. J. Cava, Proc. Natl. Acad. Sci. USA 2015, 112, E7048.
- [17] A. Perrin, C. Perrin, Eur. J. Inorg. Chem. 2011, 2011, 3848.
- [18] R. Chevrel, M. Sergent, Crystal Chemistry and Properties of Materials with Quasi-One-Dimensional Structures, Springer, Dordrecht, The Netherlands 1986, p. 315.
- [19] V. Fedorov, A. Mishchenko, V. Fedin, Russ. Chem. Rev. 1985, 54, 408.
- [20] L. Leduc, A. Perrin, M. Sergent, Acta Crystallogr., Sect. C: Cryst. Struct. Commun. 1983, 39, 1503.
- [21] X. Zhong, K. Lee, B. Choi, D. Meggiolaro, F. Liu, C. Nuckolls, A. Pasupathy, F. De Angelis, P. R. Batail, X. Roy, X. Zhu, *Nano Lett.* 2018, 18, 1483.

www.advancedsciencenews.com www.afm-journal.de

- [22] B. Choi, K. Lee, A. Voevodin, J. Wang, M. L. Steigerwald, P. Batail, X. Zhu, X. Roy, J. Am. Chem. Soc. 2018, 140, 9369.
- [23] C. Perrin, M. Potel, M. Sergent, Acta Crystallogr., Sect. C: Cryst. Struct. Commun. 1983, 39, 415.
- [24] K. S. Novoselov, D. Jiang, F. Schedin, T. J. Booth, V. V. Khotkevich, S. V. Morozov, A. K. Geim, *Proc. Natl. Acad. Sci. USA* 2005, 102, 10451.
- [25] G. Eda, H. Yamaguchi, D. Voiry, T. Fujita, M. Chen, M. Chhowalla, Nano Lett. 2011, 11, 5111.
- [26] A. J. Stapleton, C. J. Shearer, C. T. Gibson, A. D. Slattery, J. G. Shapter, Nanotechnology 2016, 27, 125704.
- [27] J. P. Perdew, K. Burke, M. Ernzerhof, Phys. Rev. Lett. 1996, 77, 3865.
- [28] J. Heyd, G. E. Scuseria, M. Ernzerhof, J. Chem. Phys. 2003, 118, 8207.
- [29] B. Kiraly, N. Hauptmann, A. N. Rudenko, M. I. Katsnelson, A. A. Khajetoorians, Nano Lett. 2017, 17, 3607.
- [30] X. Xu, Q. Song, H. Wang, P. Li, K. Zhang, Y. Wang, K. Yuan, Z. Yang, Y. Ye, L. Dai, ACS Appl. Mater. Interfaces 2017, 9, 12601.
- [31] J. Wu, N. Mao, L. Xie, H. Xu, J. Zhang, M. Han, S. Xu, Y. Xie, Y. Wu, X. Wang, Angew. Chem., Int. Ed. 2015, 54, 2366.
- [32] S. Huang, Y. Tatsumi, X. Ling, H. Guo, Z. Wang, G. Watson, A. A. Puretzky, D. B. Geohegan, J. Kong, J. Li, T. Yang, R. Saito, M. S. Dresselhaus, ACS Nano 2016, 10, 8964.
- [33] Q. Song, X. Pan, H. Wang, K. Zhang, Q. Tan, P. Li, Y. Wan, Y. Wang, X. Xu, M. Lin, X. Wan, F. Song, L. Dai, Sci. Rep. 2016, 6. 1.
- [34] Y. Liu, Q. Gu, Y. Peng, S. Qi, N. Zhang, Y. Zhang, R. Zhu, L. Tong, J. Feng, Z. Liu, J. Chen, Adv. Mater. 2018, 30, 1706402.
- [35] E. Kroumova, M. I. Aroyo, J. M. Perez-Mato, A. Kirov, C. Capillas, S. Ivantchev, H. Wondratschek, *Phase Transitions* 2003, 76, 155

- [36] H. B. Ribeiro, M. A. Pimenta, C. J. S. De Matos, R. L. Moreira, A. S. Rodin, J. D. Zapata, E. A. T. De Souza, A. H. Castro Neto, ACS Nano 2015, 9, 4270.
- [37] M. Li, Y. Wu, T. Li, Y. Chen, H. Ding, Y. Lin, N. Pan, X. Wang, RSC Adv. 2017, 7, 48759.
- [38] L. Li, P. Gong, W. Wang, B. Deng, L. Pi, J. Yu, X. Zhou, X. Shi, H. Li, T. Zhai, ACS Nano 2017, 11, 10264.
- [39] C. Hamaguchi, Basic Semiconductor Physics, Springer, Berlin, Germany 2010.
- [40] R. R. Establishment, G. Malvern, Proc. R. Soc. London, Ser. A: Math. Phys. Sci. 1963, 275, 212.
- [41] X. Ling, S. Huang, E. H. Hasdeo, L. Liang, W. M. Parkin, Y. Tatsumi, A. R. T. Nugraha, A. A. Puretzky, P. M. Das, B. G. Sumpter, D. B. Geohegan, J. Kong, R. Saito, M. Drndic, V. Meunier, M. S. Dresselhaus, *Nano Lett.* 2016, 16, 2260.
- [42] N. Mao, J. Wu, B. Han, J. Lin, L. Tong, J. Zhang, Small 2016, 12, 2627.
- [43] F. W. Koknat, T. J. Adaway, S. I. Erzerum, S. Syed, *Inorg. Nucl. Chem. Lett.* 1980, 16, 307.
- [44] G. M. Sheldrick, Acta Crystallogr., Sect. C: Struct. Chem. 2015, 71, 3.
- [45] G. M. Sheldrick, Acta Crystallogr., Sect. A: Found. Crystallogr. 2008, 64, 112.
- [46] O. V. Dolomanov, L. J. Bourhis, R. J. Gildea, J. A. K. Howard, H. Puschmann, J. Appl. Crystallogr. 2009, 42, 339.
- [47] P. Giannozzi, S. Baroni, N. Bonini, M. Calandra, R. Car, C. Cavazzoni, D. Ceresoli, G. L. Chiarotti, M. Cococcioni, I. Dabo, A. Dal Corso, S. de Gironcoli, S. Fabris, G. Fratesi, R. Gebauer, U. Gerstmann, C. Gougoussis, A. Kokalj, M. Lazzeri, L. Martin-Samos, N. Marzari, F. Mauri, R. Mazzarello, S. Paolini, A. Pasquarello, L. Paulatto, C. Sbraccia, S. Scandolo, G. Sclauzero, A. P. Seitsonen, A. Smogunov, P. Umari, R. M. Wentzcovitch, J. Phys.: Condens. Matter 2009, 21, 395502.